Optical antennas with sinusoidal modulation in width

DIRK JAN DIKKEN,* FRANS B. SEGERINK, JEROEN P. KORTERIK, STEFAN S. PFAFF, JORD C. PRANGSMA, AND JENNIFER L. HEREK

Optical Sciences Group, MESA+ Institute for Nanotechnology, University of Twente, 7500 AE Enschede, The Netherlands

*d.j.w.dikken@utwente.nl

Abstract: Small metal structures sustaining plasmon resonances in the optical regime are of great interest due to their large scattering cross sections and ability to concentrate light to subwavelength volumes. In this paper, we study the dipolar plasmon resonances of optical antennas with a constant volume and a sinusoidal modulation in width. We experimentally show that by changing the phase of the width-modulation, with a small 10 nm modulation amplitude, the resonance shifts over 160 nm. Using simulations we show how this simple design can create resonance shifts greater than 600 nm. The versatility of this design is further shown by creating asymmetric structures with two different modulation amplitudes, which we experimentally and numerically show to give rise to two resonances. Our results on both the symmetric and asymmetric antennas show the capability to control the localization of the fields outside the antenna, while still maintaining the freedom to change the antenna resonance wavelength. The antenna design we tested combines a large spectral tunability with a small footprint: all the antenna dimensions are factor 7 to 13 smaller than the wavelength, and hold potential as a design element in meta-surfaces for beam shaping.

References and links

1. L. Novotny and N. van Hulst, "Antennas for light," Nature **5**(2), 83–90 (2011).
2. P. Bharadwaj, B. Deutsch, and L. Novotny, "Optical antennas," Adv. Opt. Photonics **1**(3), 438 (2009).
3. P. Biagioni, J. Huang, and B. Hecht, "Nanoantennas for visible and infrared radiation," Rep. Prog. Phys. **75**(2), 024402 (2012)
4. A. Kinkhabwala, Z. Yu, S. Fan, Y. Avlasevich, K. MÃijllen, and W. E. Moerner, "Large single-molecule fluorescence enhancements produced by a bowtie nanoantenna," Nat. Photonics **3**(11), 654–657 (2009).
5. P. Zijlstra, P. M. R. Paulo, and M. Orrit, "Optical detection of single non-absorbing molecules using the surface plasmon resonance of a gold nanorod," Nat. Nanotechnology **7**, 379–382 (2012).
6. J. Dorfmüller, D. Dregely, M. Esslinger, W. Khunsin, R. Vogelgesang, K. Kern, and H. Giessen, "Near-field dynamics of optical Yagi-Uda nanoantennas," Nano Lett. **11**(7), 2819–2824 (2011).
7. P. Mühlschlegel, H.-J. Eisler, and O. J. F. Martin, B. Hecht, and D. W. Pohl, "Resonant optical antennas," Science **308**(5728), 1607–1609 (2005).
8. N. Yu, P. Genevet, M. A. Kats, F. Aieta, J. P. Tetienne, F. Capasso, and Z. Gaburro, "Light propagation with phase discontinuities," Science **334**(6054), 333–337 (2011).
9. X. Ni, N. K. Emani, A. V. Kildishev, A. Boltasseva, and V. M. Shalaev, "Broadband light bending with plasmonic nanoantennas," Science **335**(6067), 427 (2012).
10. H. A. Atwater, and A. Polman, "Plasmonics for improved photovoltaic devices," Nat. Mater. **9**(3), 205–213 (2010).
11. N. Berkovitch, P. Ginzburg, and M. Orenstein, "Concave plasmonic particles: broad-band geometrical tunability in the near-infrared," Nano Lett. **10**(4), 1405–1408 (2010).
12. I. D. Mayergoyz, D. R. Fredkin, and Z. Zhang, "Electrostatic (plasmon) resonances in nanoparticles," Phys. Rev. B **72**(15), 155412 (2005).
13. C. F. Bohren, and D. R. Huffman, "Absorption cross-section maxima and minima in IR absorption bands of small ionic ellipsoidal particles," Appl. Opt. **20**(6), 959–962 (1981).
14. A. Moroz, "Depolarization field of spheroidal particles," J. Opt. Soc. Am. B: Opt. Phys. **26**(3), 517 (2009).
15. E. Massa, S. A. Maier, and V. Giannini, "An analytical approach to light scattering from small cubic and rectangular cuboidal nanoantennas," New J. Phys. **15**, 063013 (2013).
16. L. Novotny, "Effective wavelength scaling for optical antennas," Phys. Rev. Lett. **266802**(6), 1–4 (2007).

17. J.S. Huang, V. Callegari, P. Geisler, C. Bruning, J. Kern, J. C. Prangsma, X. Wu, T. Feichtner, J. Ziegler, P. Weinmann, M. Kamp, A. Forchel, P. Biagioni, U. Sennhauser, and B. Hecht, " Atomically flat single-crystalline gold nanostructures for plasmonic nanocircuitry," Nat Commun **1** 150 (2010).
18. M. Agio and A. Alú, *Optical Antennas* (Cambridge University Press, 2013).
19. M. Kuttge, E.J.R. Vesseur, J. Verhoeven, H.J. Lezec, H.A. Atwater, and A. Polman. "Loss mechanisms of surface plasmon polaritons on gold probed by cathodoluminescence imaging spectroscopy," Appl. Phys. Lett. **93**, 113110 (2008).
20. C. Kan, X. Zhu, and G. Wang, "Single-crystalline gold microplates: synthesis, characterization, and thermal stability," J. Phys. Chem. B **10**(110), 4651–4656 (2007).
21. Calculations where performed using CST microwave studio.
22. P. B. Johnson and R. W. Christy, "Optical constant of the noble metals," Phys. Rev. B **6** 4370–4379 (1972)
23. E. Prodan and P. Nordlander, "Plasmon hybridization in spherical nanoparticles," J. Chem. Phys. **120**, 5444–5454 (2004)
24. L. Novotny and B. Hecht, *Principles of Nano-optics* (Cambridge University Press, 2008)
25. F. Wang, Y. R. Shen, M. S. Division, and L. Berkeley, "General properties of local plasmons in metal nanostructures," Phys. Rev. Lett. **206806**, 1–4 (2006)

1. Introduction

Optical antennas are small, wavelength-scale metal elements that convert light from the far-field into localized energy in the near-field, or vice versa [1–3]. As such, they can be used, for instance to modify the emission and absorption of quantum emitters [4], increase the response of refractive index based sensing [5, 6], or enhance non-linear optical effects [7]. They are also very effective, polarization sensitive, scatterers for light. This property for instance enables the manipulation of the phase front of propagating light to obtain tailored optical beams [8, 9], or can be used to enhance absorption in photovoltaic devices [10].

In almost every application of optical antennas, control over the spectrum is critical. In addition to this, many applications require near-field electric field enhancement. Therefore, a large effort has been put in finding handles to control these two properties, based on the geometric shape of the antenna [11, 12]. Unfortunately, only for a few simple geometries analytic expressions are available, namely for ellipsoids within the quasi-static approximation [13, 14], with extensions based on this to describe for instance cubic shapes [15]. Semi-analytical descriptions, such as the effective wavelength scaling [16], are successful in describing the spectral properties. Despite the fact that we restrict ourselves here to the simplest class of antennas that exhibit dipolar resonances and are considerably smaller than the wavelength of light, such that effectively an electrostatic problem has to be solved, there is a clear lack of engineering rules. The absence of engineering design rules that relate shape with spectrum and near-field, clearly merits the further exploration of the influence of shape on the antenna properties.

In this paper, we study both experimentally and theoretically the spectral behavior and near-field distributions of an antenna design that exhibits dipolar resonances which can be tuned over a large spectral range. The studied optical antennas are essentially a rectangular box with a sinusoidal modulation of its width, as illustrated in Fig. 1. The volume and footprint, defined as the cross sectional area, and distribution of widths, all remain constant. The only two variations between the structures we will study are (1) the phase of the cosine with respect to start and end of the particle and (2) the amplitude of the sinusoidal modulation. The structures show a smooth transition from convex to concave with decreasing modulation phase value. The experimental results we obtain, nicely portray how small changes in the shape of an antenna lead to resonance wavelength shifts, spanning 160 nm from 660 nm to 830 nm, while keeping the antenna compact in size, with both width and height below 100 nm. Using this simple design, we numerically show how the resonance wavelength can be tuned over a spectral range of 600 nm. The flexibility of this design is further shown by introducing two different modulation amplitudes on either longitudinal sides of the antenna which we experimentally and numerically show to give rise to two resonances. We furthermore discuss the applicability of a known design rule for concave

Different geometries

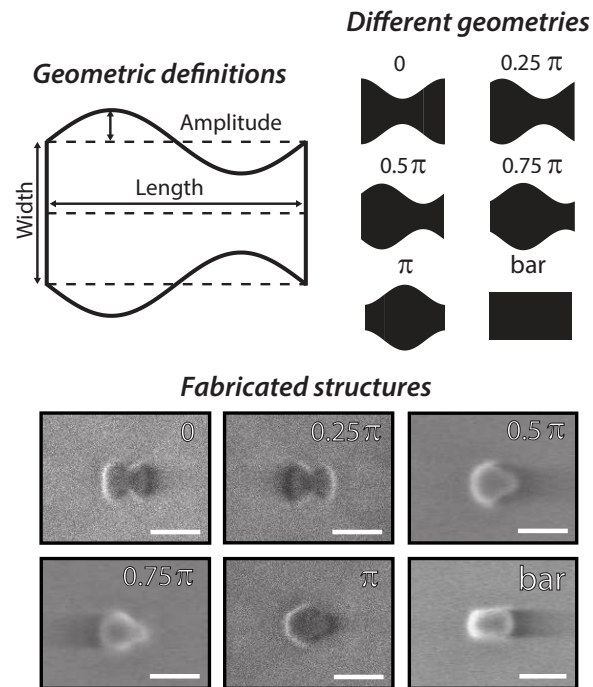*Geometric definitions*

Fabricated structures

Fig. 1. Illustrations of the studied structure. (Top left) a graphical depiction of the top view of the investigated structure, with the different geometrical definitions used in this paper. (Top right) the different geometries studied in this paper, which are obtained by changing the phase value of the sinusoidal modulation which describes the width of the antennas. (Below) SEM micrographs of an unmodulated bar and 5 width modulated nanoantennas, having different respective modulation phase values and an amplitude of 10 nm. The scale bar indicates a length of 100 nm.

antenna shapes, and we discuss the relation between the near-field distributions of the antennas and their spectral response.

2. Methods

2.1. Fabrication

The structures used in the experiments have the same volume as a reference bar antenna: 100 ±10 nm long, 70 ±10 nm wide and 35 ±10 nm high. Five types of modulated antennas have been made, with a modulation phase varying between 0 and π and a structural-modulation amplitude of 10 nm. The width modulated antennas are made using focused ion beam (FIB) milling. Single crystalline gold micro-plates are used as a uniform substrate to perform FIB milling, which has been shown to result in higher fabrication precision [17, 18] compared to multi crystalline gold films. Secondly it has been shown that due to the absence of grain boundaries, structures made from this material show lower Ohmic losses [19]. The single crystalline gold flakes are produced using the method described in [20]. Due to the small dimensions of the antennas in combination with the small feature sizes of the antenna designs, the fabrication process using the FIB suffers from both redeposition and thermal effects, leading initially to large fabrication errors. Redeposition of milled material introduces a random factor in the fabrication process. Local heating of the substrate during the FIB milling process affects the fabrication process in two ways. Firstly, local heating of the substrate increases the mobility of the atoms of the

substrate and less energy is needed to remove them, thus reducing the effective dose needed. This effect often becomes apparent when the milling sequence follows a corner, where more material is removed as a result of local heating. Secondly, when dealing with small structures and thus small volumes, strong heating of the local material will result in poor resolution, as the heated metal has the tendency to take the thermodynamically most favorable shape, which is a sphere-like structure.

Scanning electron micrographs

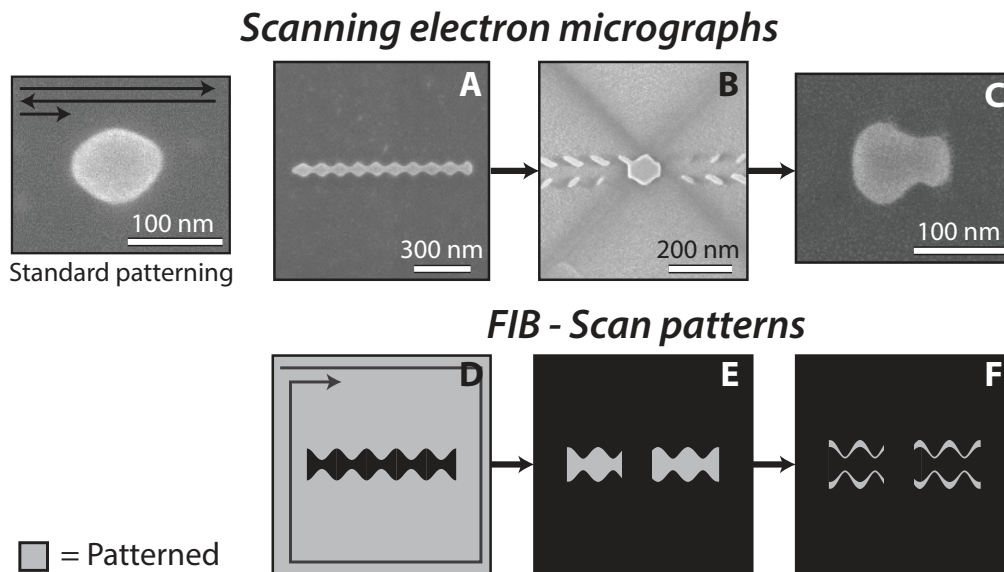## FIB - Scan patterns

= Patterned

Fig. 2. Fabrication of the modulated antennas. (Left) SEM micrograph of a nanostructure, made with a standard patterning scheme and to its right SEM micrographs of substructures (A-C), which are made during a three step FIB patterning, which are shown in (D-F). First a modulated rod of ten periods is made (A,D), after which the majority of the rod is removed, leaving a section of one period (B,E). An extra cleaning step is performed, which removes redeposited material near the structure (C,F). The structure in (B) nicely illustrates the residual material around the antenna after the second patterning step, however we note that a structure with a modulation phase of π instead of 0.5π (as in C) is shown.

We first used the standard serpentine FIB patterning technique. In this method the ion beam is raster scanned over the surface for instance with the fast axis horizontal and the slow axis vertical. To enable patterning the beam is 'blanked' at designated positions. The designed width modulated antenna structures, which where fabricated with this standard patterning technique show strong deformations with rounded end facets and low detail on the upper and lower surfaces, see Fig. 2 left panel. To address the local heating and redeposition artifacts, a more sophisticated three-step FIB pattern is applied in which the serpentine scanning routine is replaced by a inwards-spiral scanning routine. Because of the inwards-spiral scanning pattern, the area around the designed structure is patterned last, resulting in a strong reduction of redeposition effects. Local deformation due to heating effects is reduced because the final structure is now more evenly heated from all sides, see Fig. 2(d). First, a long sinusoidal-modulated rod is made Fig. 2(d), which is shortened in the second step (E), and finally the residual material is removed (F). The final result, see Fig. 2(c), shows a significant improvement compared to the structure made with the standard serpentine FIB patterning.

2.2. Experimental setup

The experimental spectral analysis of the antennas is done using a dark-field micro-spectrometer, see Fig. 3, which is capable of obtaining a spectrum of each individual antenna. It is then possible to directly relate the geometry of the antenna with its spectral response. For the antennas studied in this paper, it is crucial to measure individual antennas as small geometry changes can lead to large changes in resonance wavelength. The dark-field spectroscopy setup uses the white light
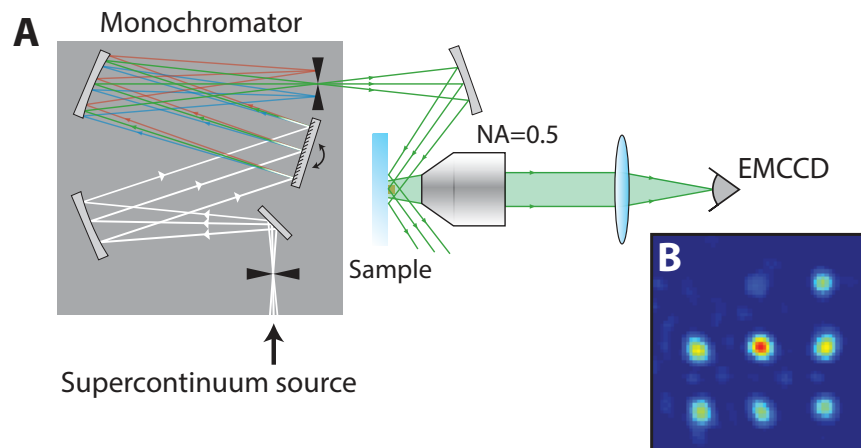

Fig. 3. Dark-field spectroscopy setup. A) schematic of the dark-field spectroscopy setup: a supercontinuum source is coupled into a monochromator after which a beam with a 2 nm spectral bandwidth is focused onto the sample under an angle of approximately 50° with respect with the substrate. A 0.5 NA objective collects the light emitted from the nanostructures, after which it is focused on a cooled electron multiplying (EM) CCD. B) Typical dark-field image collected by the EMCCD camera, which in this case shows the scattering of 9 bar antennas of different lengths which are illuminated at $\lambda = 710$ nm.

from a supercontinuum source (Fianium SC400-4) which is passed through a monochromator (Acton SP-2100i) to select the center wavelength of the illumination light with a 2 nm spectral bandwidth. The light is linearly polarized and focused weakly onto the sample under an angle of 50 degrees with respect to the substrate. While sweeping the monochromator output through the frequency range of interest, a series of images are collected on an EMCCD camera (Andor Ixion 878), using a 0.5 NA long working distance objective. We compensate for the chromatic shift in the focus of the collection objective by translating the sample stage during our measurements. This process is automated and before each measurement a calibration is made where the focus is determined at eight different wavelengths. A polynomial fit on the eight measurements is done, which is then used for positioning the sample stage during the measurement. Typically a maximum stage movement of approximately 15 μm is needed for the objective which is used. The size of the illumination spot (ellipse with a long and short radius of approximately 500 and 200 micrometers) was chosen such that the slight automated translation of the sample stage, during the experiment, does not result in a measurable modulation of illumination intensity. At any given point in the field of view ($\pm$ 50x50 μm), a spectrum is obtained by acquiring images at a range of different frequencies. The spectra are normalized by the spectral response of the system, which is obtained by measuring the scattering from a diffuser element.

3. Results

3.1. Modulation phase

The effect of the phase value of the width modulated optical antennas and the resulting resonance wavelength shift is depicted in Fig. 4. Panel A shows experimental scattering spectra of an unmodulated bar antenna (in blue) having a resonance wavelength at 740 nm, and five width modulated antennas with modulation phases varying between 0 and π having a modulation amplitude of 10 nm. The experimental scattering spectra of individual antennas are obtained using the dark-field spectroscopy setup. The excitation source is linearly polarized and orientated along the long axis of the antennas. A single resonance peak is observed for each of the modulated antennas, and as the modulation phase value changes from 0 to π, a monotonic decrease in resonance wavelength is observed from 830 to 670 nm. The total range of resonance wavelengths that can be achieved with this collection of structures is approximately 160 nm. Finite element method calculations [21] of the structures where calculated and are depicted Fig. 4(b). For optical antennas the dielectric constants of gold are used which are obtained from the experimental data of Johnson an Christy [22], which are fitted with a 4th order polynomial. The optimum mesh size and boundary conditions where checked such that they did not alter the obtained spectral response. The experiments show a 20 nm larger red shift and a 10 nm smaller blue shift in comparison to the calculations, these small differences are attributed to small fabrication imperfections.

The electric field distributions of the width-modulated antennas are of interest in many sensing applications where field localization is of importance. The possibility to manipulate the near-field distribution of the nanoantenna is therefore of large importance. Panels (C-G) of Fig. 4 show numerical calculations of the electric field distribution of width modulated antennas with different modulation phases and a modulation amplitude of 20 nm. The electric field distributions are all in the same color scale and are obtained at their respective resonance frequency. In the lower left corner of each figure, the value of the average electric field amplitude outside the metal inside a 225 by 225 nm area is shown as an indication of the relative near-field enhancements of the different geometries. It can be seen that the concave structure with a modulation phase of 0 has 1.9 times higher near-field than the convex structure with a modulation phase of π, with the other values in between following a monotonic decrease with modulation phase value. The concave structures show a field distribution which is localized more towards the concave center, in comparison to the convex structures, where the fields are more localized towards the end-facets of the antenna. Also, with increasing modulation phase values the field distributions become asymmetric in the sense that the left half of the antenna shows higher field concentration compared to the right half. In the case of a 0.75 π modulation phase, the field amplitude on the left half of the antenna is almost 2 times stronger compared to the right half. We later will show that the electric field distributions are directly related to the resonance behavior of the antennas.
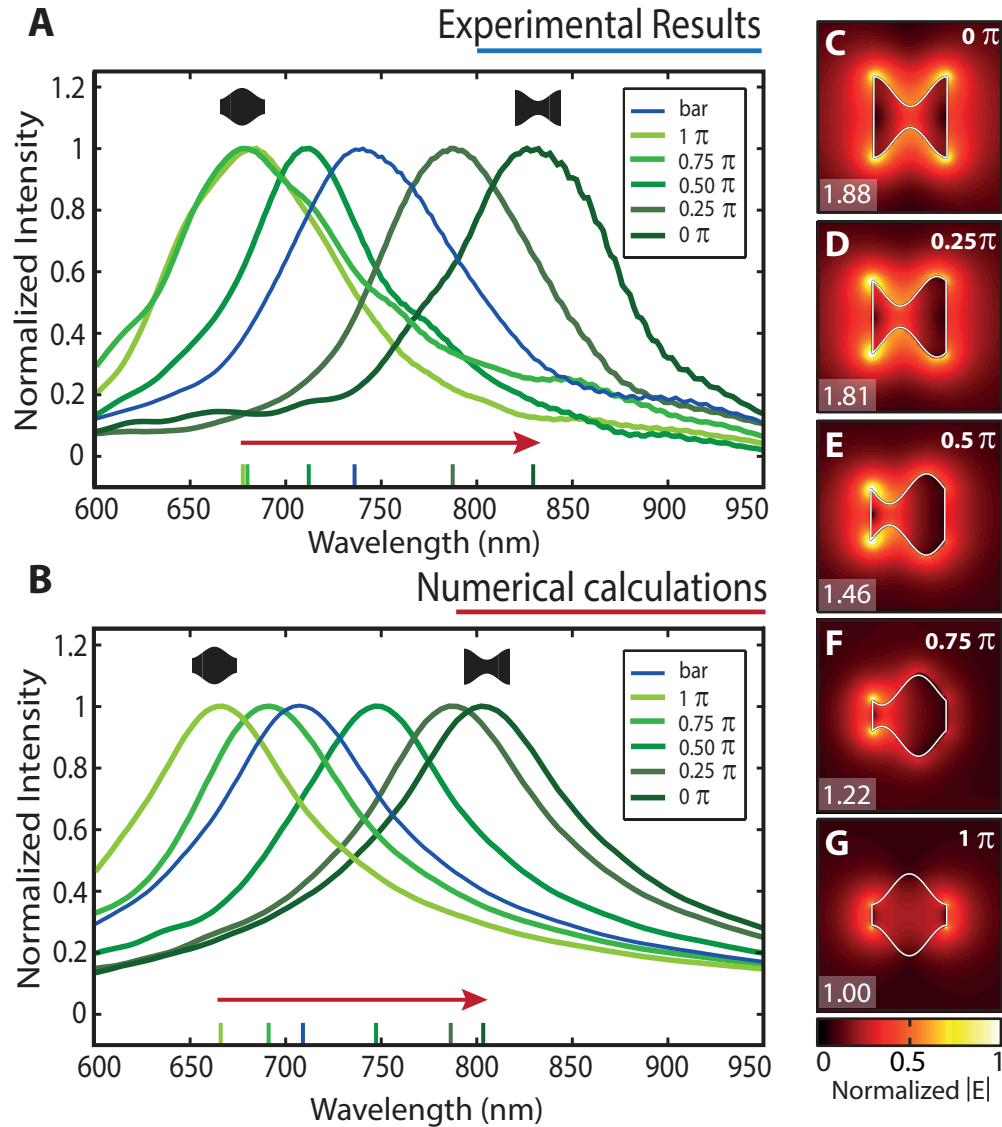
Fig. 4. Scattering spectra of width modulated antennas with various modulation phases. (A) experimental data, (B) numerical calculations showing scattering spectra of width modulated antennas having different respective modulation phase shifts and an modulation amplitude of 10 nm. The scattering spectra are normalized to their respective maximum intensity. The maximum scattering intensities of the various antenna shapes have shown to be of approximately equal magnitude. (C-G) numerically calculated absolute electric field distributions of 5 modulated antennas with different modulation phases and a modulation amplitude of 20 nm. The electric field distributions have been normalized to the same value and a ratio of the overall cumulative electric field distribution outside the metal, is shown in the bottom left corner of each respective image.

3.2. Modulation amplitude

The relation between the observed resonance shifts and modulation amplitude of the antenna is further investigated numerically. Figure 5 shows the resonance wavelength as a function of modulation amplitude, varying from 0 nm, which is equal to an unmodulated bar antenna, to 30 nm, in which case the maximum and minimum width of the antenna are 130 and 10 nm, respectively. The resonance wavelengths are extracted from numerically calculated scattering spectra. By changing the amplitude in the sinusoidal modulation, the resonance wavelength can be tuned over a spectral range exceeding 600 nm. This is an exceptionally large effect and in order to obtain a similar resonance shift in the ordinary bar antenna, one would have to increase its length by a factor of 2.8, from 100 to 280 nm. Figure 5 shows a similar trend as seen in Fig. 4, in which the resonance wavelength of the modulated antenna is redshifting for a decreasing modulation phase from π to 0. However, by incorporating the modulation amplitude, it becomes clear that the effect resulting in a blue shift is relatively small in comparison to the effect leading to a redshift. This becomes even more evident in the case of an antenna with a modulation phase of 0.75π, which for modulation amplitudes up to 15 nm experiences a blue shift, while a red shift is seen at larger modulation amplitudes. Its interesting to note that the resonance wavelength at a modulation amplitude of 17.5 nm is exactly the same as an unmodulated bar antenna, which might indicate the presence of two competing processes. As a result of this, Fig. 5 displays how modulated antennas having varying modulation phase and amplitude have similar resonance wavelengths while having different (a)symmetric field distributions.
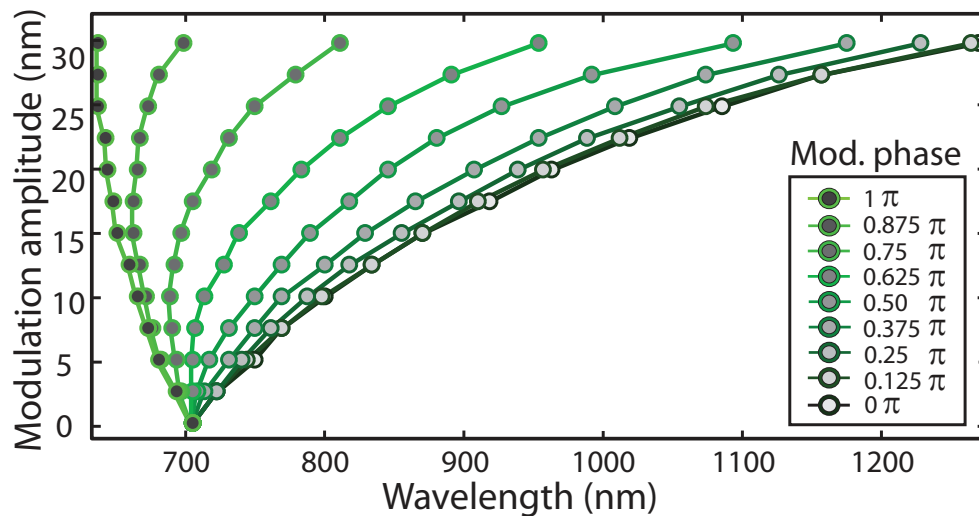

Fig. 5. The effect of modulation amplitude and phase on resonance wavelength. Numerical calculations of various width modulated antennas and their respective resonance wavelength. The resonance wavelength of the nine different types of modulated antennas, having different modulation phases, are calculated for various modulation amplitudes.

3.3. Asymmetric modulations

Finally we investigate how the antenna resonances change if the two sides of the antenna have a different sinusoidal modulation amplitude, thus introducing an asymmetry in the antenna. The starting structure is a modulated antenna having a modulation phase of 0. The asymmetry is realized by shifting the center section of the antenna, in order to preserve the volume for the different contour shapes. Figure 6(a) shows one experimental and several numerical scattering

spectra of antennas with different degrees of asymmetry in their respective contour shapes. The antennas, having a center shift of 0 to 30 nm, change from a fully symmetric antenna to an antenna with a large asymmetry, where one of the sides is flat. The fabricated asymmetric antenna has a center shift of 10 nm. The numerical scattering spectra reveal that, upon introducing asymmetry in the contour shape, the single resonance peak of the symmetric structure is significantly redshifting, as can be expected based on the effect of amplitude of the modulation we found for the symmetric antennas. A second peak emerges around 700 nm, which is blue shifting with increasing asymmetry. The two resonance peaks are clearly observed in our experimental scattering spectra, although both peaks are slightly more blue shifted. The near-field distributions of the two modes of an asymmetric modulated antenna with a center shift of 20 nm are shown in Figs. 6(b) and 6(c) at their resonance wavelengths λ_{res} = 690 nm and λ_{res} = 980 nm. It can be seen that the near-field distributions of both the resonances are predominantly localized on either sides of the modulated antenna, where the shorter and longer wavelength resonance are localized on the side with smaller and larger modulation amplitude, respectively. Figure 6(c) illustrates that the field distribution now becomes asymmetric, and the fields get more concentrated on the side with the larger modulation amplitude.
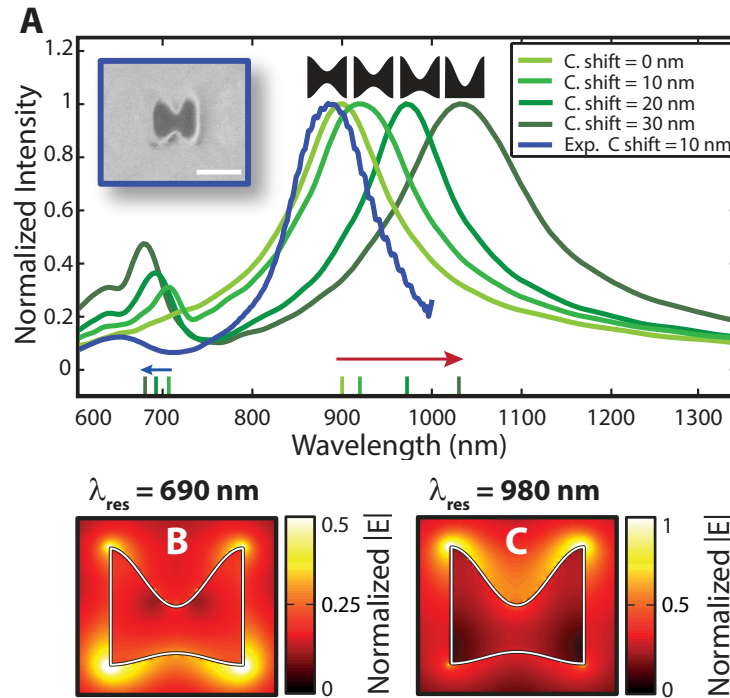

Fig. 6. Asymmetric width modulated antennas. (A) experimental and numerical scattering spectra of asymmetric width modulated antennas, having different degrees of asymmetry due to a vertical shift of the center section. The calculations have been done for a starting modulation amplitude of 15 nm. The experimental scattering spectra shows a cutoff at 1000 nm due to low signal-to-noise of the used EMCCD. Micrograph showing a SEM image of the experimented structure, with a white bar indicating 100 nm. (B-C) numerically calculated electric field distributions of an asymmetric width modulated antenna, with a center shift of 20 nm at λ_{res} = 690 nm and λ_{res} = 980 nm. The electric field distributions are normalized to the maximum value of figure (C).

4. Discussion

4.1. Fredholm integral

In an earlier study on concave and convex shaped optical antennas [11], the resonance behavior of the different antenna shapes was explained by means of a surface integral eigenvalue based technique. There it was proposed that the different resonance behavior of concave and convex antennas can be related to the combination of their geometrical shape and their charge distribution upon excitation. The geometry dependent eigensolution for the surface charge density and the eigenvalues, which describe the resonance frequency of the antenna, are found using the Fredholm integral equation [12], which here is shown in its two dimensional form:

$$\sigma(Q) = \frac{\epsilon(\omega) - 1}{\epsilon(\omega) + 1} \int_S \sigma(M) \frac{\vec{r}_{MQ} \cdot \hat{n}_Q}{\pi |\vec{r}_{MQ}|^2} \cdot dS_M \qquad (1)$$

where $\sigma(Q)$ is a surface charge density at point Q, and $\epsilon(\omega)$ is the dielectric constant of the antenna material. The integration is performed on the surface of the antenna, where $\vec{r}_{MQ}$ describes the vector which connects any point (M), on the antenna surface with a point of interaction (Q) and $\hat{n}_Q$ is the normal to the surface at the point Q, see Fig. 7. In order to obtain the resonance
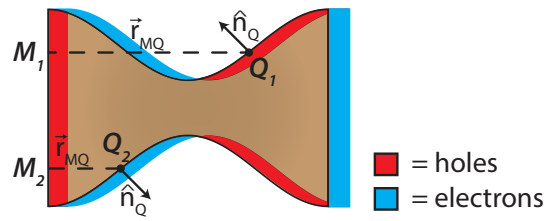

Fig. 7. Fredholm integral method. Cartoon depicting the Fredholm integral method applied on two positions on the surface of a concave antenna. The red and blue areas indicate the accumulation and depletion of charge, due to the oscillatory movement of the free electrons.

frequency of an antenna, a full numerical calculation, solving the eigen-value problem given by the Fredholm surface integral, the surface charge distribution is required [12]. A conceptual explanation of the resonance shifts is provided in [11], where it is pointed out that for concave particles, the normal to the surface can point in a counter direction to the charge separation vector, which thus results in a local negative value of the scalar product within the integrand of Eq. 1, indicated with situation 1 in Fig. 7 (M_1, Q_1). It is then argued that because of these negative values in the surface integral, which occur in the concave and not in the convex antennas, a resonance red-shift is expected. Although this method of acquiring the resonance behavior of an optical antenna, described in [12], has proven to be generally valid, the conceptual explanation provided in [11] actually leads to a blueshift instead of a redshift. This is exemplified in Fig. 7, where two points on the antenna surface are investigated, which lie closer together (M_2, Q_2). In this case, the scalar product in the integrand will lead to a positive contribution, which actually is of a larger magnitude than situation one, as $\vec{r}_{MQ}$ in this case is smaller, and using the same line of thought would lead to a blueshift rather than a redshift. We conclude from this that although the Fredholm integral method is capable of calculating the resonance behavior of optical antennas when the field distribution is known, it fails to provide easy insight in the general relation between the shape of an antenna and it spectrum.

4.2. The relation between E-fields and ϵ of an antenna

The numerical results depicted in Fig. 4 show a monotonic scaling of field enhancement and of the resonance wavelength. It is therefore interesting to consider whether or not an independent

optimization of the average field-enhancement and spectrum is possible. Wang et al. [25] derived as a general property of plasmon resonances in the quasi-static limit, a relation between the ratio of integrated fields in Ω_m and outside Ω_d the antenna and the dielectric constants:

$$-Re\left\{\epsilon_m(\omega)\right\}/\epsilon_d = \int_{\Omega_d} \overline{E^2} dV \; / \; \int_{\Omega_m} \overline{E^2} dV \qquad (2)$$

Here ϵ_m and ϵ_d are the dielectric constant of the metal and dielectric, respectively. The real part of the dielectric constant of metal, such as gold and silver, is negative and monotonically decreasing with wavelength. Therefore relation (2) signifies that for structures that have the same volume, a redshift corresponds to a relatively lower penetration of the field into the metal, and/or a higher field outside the material. We tested this relationship for our calculated antennas with all modulation phase values and amplitudes, by integrating the square of the electric field in the cross-sectional surface, as depicted in Figs. 4(a)–4(e). Though the equality in Eq. 2 holds only for the volume integrated fields, a linear proportionality is expected to hold for the fields in the cross section area. Figure 8 depicts the relationship which is indeed found to be linear up to a reasonable level, indicated by the blue dashed line, which shows a linear fit of the data points. The antenna shapes which lie above the fitted line, are those which show a strong intensity ratio $\overline{E^2}_{dielectric}/\overline{E^2}_{metal}$, which are associated with the concave antenna shapes. Deviations can be attributed to several factors. Firstly the linear relationship is derived for the quasi-static approximation. Our FDTD calculations are using full retardation effect into account. The geometries we calculate on are 5 to 10 times smaller than the wavelength and thus it is reasonable to assume some deviations can be attributed to deviations from a quasi-static case. Secondly some deviations could be related to numerical limitations in our simulations. It is well known that strongly curved surfaces are difficult to simulate accurately, leading to non-physical strong local fields. However, it seems this combined effect of these deviations is relatively small as the bulk of the data points follow the linear fit.

We should stress here that Eq. 2 does not contain geometric information, and thus only gives an implicit relationship between shape and spectrum or near-field. We can, however, conclude that independent tuning of near-field outside the particle and the spectrum would require substantial variation in the field inside the particle. For a particle of given volume and given the fabrication
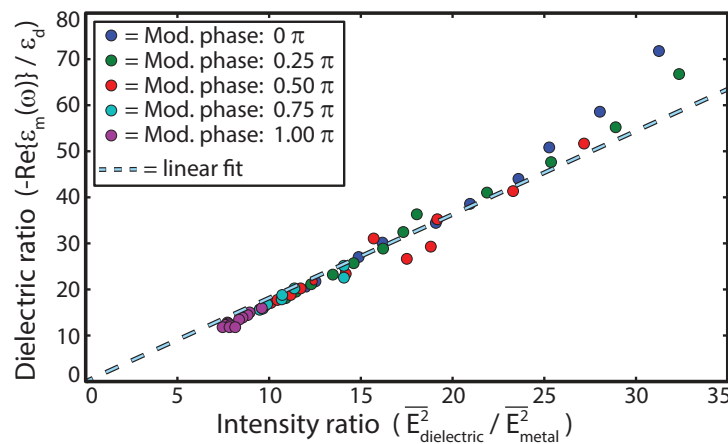

Fig. 8. Relation between E-fields and ϵ of an optical antenna. The ratio of dielectric constants in and outside the antenna, versus the ratio of the electric field in and outside the antenna, for simulated antennas with different modulation phases (0, 1/4, 1/2, 3/4, 1)π and amplitudes (0-30 nm). The dashed line shows a linear fit.

constraints, variation in the depth of penetration of fields into the structure seems to be quite limited, as most dimensions here are already on the scale of the field penetration (skin) depth ($\delta = \lambda/(2\pi\sqrt{-\epsilon'_m}) = 25$-$30$ nm). We see this confirmed in the calculations on our set of particles, thus strongly suggesting resonance wavelength and near-field ratio, in and outside the antenna, are not separately tunable. However our results on both the symmetric and asymmetric antennas show that it is possible to introduce an asymmetry in the near-fields outside the antenna, thus localizing the fields, at the resonance wavelength of the antenna. While preserving the resonance wavelength of the antenna, with our design it is possible change the localization of the near-fields outside antenna by changing either the modulation phase or center symmetry of the antenna.

5. Conclusion

We have introduced a new design for controlling the spectral behavior of optical antennas by applying a sinusoidal modulation on the long axis of an optical antenna. By changing the modulation phase, the antenna structure changes from a concave to a convex shape. From our experimental results and numerical calculations we find that the concave antenna shapes lead to a strong redshift of the resonance while a more modest blueshift results from convex antenna shapes. Our antenna design delivers the possibility to introduce a tunable amount of concaveness or convexness into an antenna shape, making it possible to tune the resonance wavelength of this antennas design over a broad spectral range of more than 600 nm. We also showed that by introducing an asymmetry in the antenna design, which is done by applying two different modulation amplitudes on both longitudinal sides of the antenna, two resonances emerge with electric field distributions that are strongly localized on the respective sides of the antenna. By using this approach it is possible to obtain an asymmetric field distribution, leading to a localization of the fields. We used our system to check a proposed relation between the resonance wavelength and the ratio of total integrated electric fields inside and outside the antenna. From this we conclude that while this relation holds, our asymmetric antennas do enable to change the field distribution. Our antenna design thus shows concrete methods to control the localization of the near-field distribution and the resonance wavelength of an antenna, both of which are key ingredients in many optical applications.

Funding